Coherent phonon generation in time-dependent density functional theory

Y. Shinohara,[1] K. Yabana,[1,2] Y. Kawashita,[1] J.-I. Iwata,[2] T. Otobe,[3] and G. F. Bertsch[4]

[1]*Graduate School of Science and Technology, University of Tsukuba, Tsukuba 305-8571, Japan*
[2]*Center for Computational Sciences, University of Tsukuba, Tsukuba 305-8571, Japan*
[3]*Advanced Photon Research Center, Japan Atomic Energy Agency, Kizugawa, Kyoto 619-0215, Japan*
[4]*Institute for Nuclear Theory and Department of Physics, University of Washington, Seattle, Washington 98195, USA*

We apply the adiabatic time-dependent density functional theory (TDDFT) to the generation of coherent optical phonons in Si crystals by intense laser pulses. The theory reproduces the main phenomena observed experimentally: dependence on polarization, strong growth at the direct band gap, and the change in phase from below to above the band gap. Both show that two mechanisms invoked in phenomenological theory, namely, impulsively stimulated Raman scattering and displacive excitation, are present in the TDDFT. The calculated phase of the coherent phonon is in qualitative agreement with experiment and with phenomenological modeling in the vicinity of the direct band gap. At higher laser frequencies, the TDDFT predicts additional structure not present in the modeling.

I. INTRODUCTION

Since its first observation in Ref. 1, coherent optical phonon generation by intense light pulses has been an active area of research and has by now been studied in many materials including insulators,[2,3] semiconductors,[4–9] metals,[10] semimetals,[11–15] ferroelectrics,[16] ferromagnets,[17] superconductors,[18] and organic media.[19] We also mention a possible application to broadband comb generation.[20] For a review of the earlier work, see Ref. 21. A number of interesting phenomena are observed in cubic crystals. The amplitude and vibrational axis of the phonon is strongly dependent on the polarization of the laser field, as expected from crystalline symmetry considerations. The phase of the vibration is found to depend sensitively on the laser frequency, varying by nearly $\pi/2$ as the threshold for direct transitions across the band gap is passed.[7]

Traditionally, phenomenological theories have been employed to describe the phonon generation.[22] Below the gap, the underlying mechanism is the stimulated Raman effect, called "impulsively stimulated Raman scattering" (ISRS) in this context.[1,23] In molecular Raman scattering, this is normally calculated by considering the polarizability function and its dependence on the vibration coordinates. In solids, the stimulated Raman effect may be treated in third-order perturbation theory[24] or in terms of the dielectric polarizability function.[25] Above the gap, the assumed mechanism, called "displacive excitation of coherent phonons"(DECP),[26–28] invokes a force on the phonon coordinates associated with persistent electron-hole excitations. A phenomenological model has also been developed to consider both mechanisms together.[7,29,30] In particular, the model by Stevens, Kuhl, and Merlin (SKM) (Ref. 30) requires only the dielectric function as input, apart from an overall factor.

In this work, we apply the time-dependent density functional theory (TDDFT) to the laser-lattice interaction and the calculation of coherent phonons. It appears that TDDFT is the only computationally feasible *ab initio* method to treat the effects of strong transient fields on systems containing many electrons, and it is important to test it in new ways, as well as to get a deeper insight into the physical process under study. In this paper we report on the first application of the method to silicon, for which there exist a number of experimental measurements.[6–8] We will show that the theory applies to both the ISRS and the DECP regimes of excitation, thus providing a comprehensive framework for treating coherent laser-lattice interactions. We note that the static DFT has already been successfully applied to calculate the needed dielectric polarizability function for a macroscopic treatment of Raman scattering in Si crystals.[31] Calculations of the full time-dependent theory have also been recently reported for the coherent phonon generation in diamond.[32]

II. PHYSICAL DESCRIPTION

We start with a brief description of the pump-probe experiments used to detect and measure the coherent phonons. The pump laser pulse is directed on a [100] Si surface at near-normal incidence. The laser field has a linear polarization, and for maximum effect, the electric field of the laser is oriented along the [011] axis (or the equivalent [01$\bar{1}$] axis). The generated coherent phonon destroys the isotropy of the dielectric tensor in Si crystal, causing the dielectric function ϵ_{ii} along the [011] axis to differ from that along the perpendicular [01$\bar{1}$] axis. The anisotropy is detected by a probe pulse having a linear polarization along the [001] or [010] axis. The electric field of the reflected pulse will be rotated by an amount that depends on the anisotropy of the dielectric tensor. The experimental results are conventionally reported in terms of the anisotropy of the reflectivities perpendicular and parallel to the electric field of the pump pulse,[6] $\Delta R_{eo} = R_\perp - R_\parallel$. Experimentally, one sees an oscillation at the frequency of the optical phonon ω_{ph}. An important observable is the phase of the oscillation with respect to the pump pulse, ϕ, in the expression,
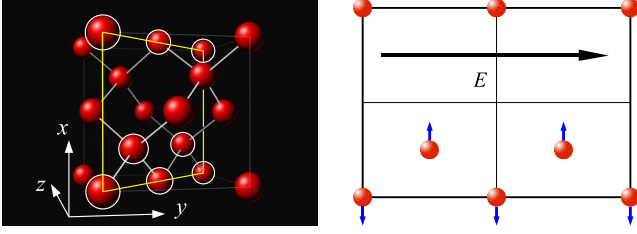
FIG. 1. (Color online) Geometry of the electric field and the optical phonon displacement in the eight-atom unit cell. On the left is shown the geometry of the cell with a cut through the [011] ×[100] plane. The atoms on the plane are highlighted in white. The plane with its atoms is shown at the right in a face view. The long arrow shows the axis of the electric field and the small arrows show the direction of the optical phonon coordinates.

$$\Delta R_{eo}(t) = \Delta R_0 \cos(\omega_{ph}t + \phi) + \Delta\bar{R}. \tag{1}$$

One also sees a shift in the equilibrium value in the experimental measurement which may be fit by adding a constant term $\Delta\bar{R}$.

The physical origin of the effect can be seen from the response to the field within a unit cell, depicted in Fig. 1. The left panel shows a view of the atoms in the eight-atom unit cell, bisected by a plane defined by the [011] and [100] axes. The four atoms lying on the plane are shown together with corresponding atoms from adjacent cells. In the right panel we show a frontal view of that plane and the atoms on it. The electric field axis is in the plane, shown by the large horizontal axis. The relevant optical phonon coordinates are shown by the vertical arrows.

There is no linear coupling between electric field and the phonon coordinates but in second order there are two ways that they may interact. The polarizability of the electrons between silicon atoms obviously changes with the separation of the atoms. As may be seen from the displacement vectors of the optical phonon, the separation between atoms with bonds in the [111] and [$\bar{1}$11] directions increase. The bonds in the [11$\bar{1}$] and [1$\bar{1}$1] directions, which are perpendicular to the plane, decrease in length. Let us call these A and B bonds, respectively. The polarizability can obviously differ along the A-bond and B-bond directions when the atoms are displaced as depicted for the optical phonon coordinate.

In the Raman mechanism, all changes in the electron wave function are assumed to be adiabatic. Considering the dielectric tensor as a function of the phonon coordinate, both the effect of the pump pulse and the response of the probe pulse can be calculated from knowledge of the macroscopic dielectric function ε_{ii} for the two perpendicular directions i =[011] and [01$\bar{1}$]. The dependence on the phonon coordinate q gives rise to the force generating the phonon as well as the change in reflectivities needed to observe it. In this mechanism, the pump pulse produces an impulsive force and the response is sinusoidal with a phase angle $\phi = \pi/2$ in Eq. (1), independent of the sign of $\partial\varepsilon_{ii}/\partial q$.

The other mechanism, displacive phonon generation, considers the effect of the internal excitations created by the pump pulse. For high-field intensity or with high-frequency laser pulses, the pump pulse creates electron-hole excitations that persist in the final state. Again, the electrons in the A and B bond regions may be excited differently, going into different orbitals in the conduction bands. The equilibrium lattice in the presence of electron-hole excitations may show a nonzero displacement in q. In that case, without any impulsive force, the phonon amplitude with respect to the new equilibrium would be maximal at $t=0$. This implies that the phase of the optical phonon would be $\phi=0$ or π.

III. FORMALISM

A. Equations of motion

The TDDFT equations for evolution of the electron wave function are based on the Lagrangian formalism presented in Ref. 33, treating the electron dynamics in solids induced by a spatially uniform electric field. The formalism has been applied to calculations of the dielectric function in linear-response regime[33] and to the description of optical dielectric breakdown in nonlinear regime.[34] For the present application, we treat the positions of the ions as additional variables in the Lagrangian, adding a kinetic term to permit classical time-dependent dynamics[35] [Eq. (4.12)]. Similar treatments of mixing classical-quantum dynamics have been used in quantum chemistry to describe molecular reactions and vibrational coupling.[36] The combined Lagrangian for the coupled electron-lattice dynamics in solids is

$$
L = \sum_i \int_\Omega d\vec{r} \left\{ \psi_i^* i\frac{\partial}{\partial t}\psi_i - \frac{1}{2m}\left|\left(-i\vec{\nabla} + \frac{e}{c}\vec{A}\right)\psi_i\right|^2 \right\}
$$
$$
- \int_\Omega d\vec{r}\{(en_{ion} - en_e)\phi - E_{xc}[n_e]\} + \frac{1}{8\pi}\int_\Omega d\vec{r}(\vec{\nabla}\phi)^2
$$
$$
+ \frac{\Omega}{8\pi c^2}\left(\frac{d\vec{A}}{dt}\right)^2 + \frac{1}{2}\sum_\alpha M_\alpha\left(\frac{d\vec{R}_\alpha}{dt}\right)^2 + \frac{1}{c}\sum_\alpha Z_\alpha e\frac{d\vec{R}_\alpha}{dt}\vec{A}. \tag{2}
$$

Here ψ_i are the time-dependent electron orbitals, taken as Bloch orbitals in a unit cell of volume Ω. The electromagnetic fields are represented by two time-dependent terms: $\vec{A}(t)$ is the spatially uniform vector potential which describes the macroscopic electric field. The field $\phi(\vec{r},t)$ is the Coulomb potential, assumed to be periodic. Also, $n_e(\vec{r},t) = \Sigma_i|\psi_i(\vec{r},t)|^2$ represents the electron-density distribution. The corresponding ion density is expressed $n_{ion}(\vec{r},t) = \Sigma_\alpha Z_\alpha\delta(\vec{r} - \vec{R}_\alpha)$ with Z_α the charge numbers and $\vec{R}_\alpha$ the coordinates of the ions. Note also in the second line of Eq. (2) the exchange-correlation term E_{xc} associated with the energy functional of DFT.

Variation of the Lagrangian with respect to ϕ immediately yields the Poisson equation for the Coulomb potential,

$$\nabla^2\phi(\vec{r},t) = -4\pi e[-n_e(\vec{r},t) + n_{ion}(\vec{r},t)]. \tag{3}$$

Variation with respect to ψ_i yields the time-dependent Kohn-Sham equation,

$$i\frac{\partial \psi_i}{\partial t} = \frac{1}{2m}\left[-i\vec{\nabla} + \frac{e}{c}\vec{A}(t)\right]^2\psi_i - e\phi\psi_i + \frac{\delta E_{xc}}{\delta n}\psi_i. \qquad (4)$$

The DFT is often carried out with a reduced number of active electrons and an ionic pseudopotential V_{ion} to take into the core electrons. It is nonlocal, giving rise to an additional term $\Sigma_i \int d\vec{r} d\vec{r}' \psi_i^*(\vec{r}) V_{ion}(\vec{r},\vec{r}') \psi_i(\vec{r}')$ in the Lagrangian and in the Kohn-Sham equation. Note that the nonlocality makes the pseudopotential gauge dependent.

Variation with respect to $\vec{A}$ yields

$$\frac{\Omega}{4\pi c^2}\frac{d^2\vec{A}(t)}{dt^2} = \frac{e}{c}\int_\Omega d\vec{r}\{\vec{j}_{ion} - \vec{j}_e\} - \frac{e^2}{mc^2}N_e\vec{A}(t),$$

where $\vec{j}_{ion}$ and $\vec{j}_e$ represent ion and electron currents, respectively, and N_e is the number of electrons in the unit cell.

To introduce the external laser field, we express the vector potential as a sum of an external field $\vec{A}_{ext}(t)$ and the induced field $\vec{A}_{ind}(t)$. All the equations of motion are the same except the dynamic equation for $\vec{A}$. It becomes

$$\frac{\Omega}{4\pi c^2}\frac{d^2\vec{A}_{ind}(t)}{dt^2} = \frac{e}{c}\int_\Omega d\vec{r}\{\vec{j}_{ion} - \vec{j}_e\} - \frac{e^2}{mc^2}N_e\vec{A}(t) \qquad (5)$$

with

$$\vec{A}(t) = \vec{A}_{ext}(t) + \vec{A}_{ind}(t). \qquad (6)$$

In the formalism for calculating the linear response,[33] the external field was imposed by a step-function change in $\vec{A}(t)$ at time $t=0$, so it was not necessary to keep the distinction between external and internal contributions for the later evolution. In this work, we simulate the time-dependent electric field of the laser pulse and take $\vec{A}_{ext}(t)$ to have the form

$$\vec{A}_{ext}(t) = \int^t dt' \vec{\mathcal{E}}_0 \sin^2\left(\frac{\pi t'}{T_p}\right)\sin \omega t' \qquad (7)$$

for $0 < t < T_p$ and zero otherwise.

Physically, the external field $\vec{A}_{ext}(t)$ defined this way corresponds to an electric field outside the medium and perpendicular to the surface, as in the geometry of a capacitor with a dielectric slab between two plates. For excitation of the medium by a laser pulse, the electric field is parallel to the surface and $\vec{A}_{ext}$ has no direct physical significance. However, we may use it to generate the full field through the equations of motion, and derive the intensity of the laser from that field strength. To make a quantitative connection, one has to take into account also the transmission of the laser beam through the interface. It is a simple exercise in electromagnetic theory to derive the needed formula; the relationship of A_{ext} to the field strength in the incident laser beam is

$$A_{ext} = \frac{2\epsilon}{1 + \epsilon^{1/2}}A_{in}. \qquad (8)$$

where A_{in} is the field strength of the laser beam in vacuum.

The remaining equation of motion is the one for the ionic coordinates $\vec{R}_\alpha$. It is given by

$$M_\alpha \frac{d^2\vec{R}_\alpha}{dt^2} = -\frac{e}{c}Z_\alpha\frac{d\vec{A}}{dt} - \frac{\partial}{\partial \vec{R}_\alpha}\int_\Omega d\vec{r} e n_{ion}\phi. \qquad (9)$$

The right-hand side is the force on the ion and is the focus objective of our study.

B. Adiabatic limit

The TDDFT theory respects the well-known adiabatic relationship between the macroscopic polarizability χ and the force on the ions, encapsulated in the formula,[22]

$$\frac{d^2q}{dt^2} + \omega_{ph}^2 q = F(t) = \frac{1}{2}\frac{\partial \chi}{\partial q}|\mathcal{E}(t)|^2, \qquad (10)$$

where q is a phonon coordinate linearly related to the ion positions $\vec{R}_\alpha$. This fundamental connection between the force and χ is not obvious from the equations of motion, Eq. (9), so we outline here a derivation. We start with the second-order expression for the electronic wave function $\Psi(t)$ in the presence of the laser field. Consider the electromagnetic field of the form $A = A_0 \sin(\omega t)$ acting as the perturbation.[22] The electronic wave function is expanded to second order as

$$\Psi(t) = e^{-i(E_0 + E_2)t}\left(\phi_0 + \sum_{n=-2}^{2} e^{-in\omega t}\Phi_{n\omega}\right), \qquad (11)$$

where E_0 is the ground-state electronic energy in the absence of the field A. $\Phi_{\pm\omega}$ and $\Phi_{0\omega}$, $\Phi_{\pm 2\omega}$ are, respectively, first- and second-order corrections to the ground-state wave function Φ_0. The second-order contribution E_2 to the overall phase of Ψ is found to be

$$E_2 = \frac{e^2 A_0^2}{4m^2c^2}\langle\Phi_0|\vec{P}\left(\frac{1}{-H + E_0 + \omega} + \frac{1}{-H + E_0 - \omega}\right)\vec{P}|\Phi_0\rangle$$

$$+ \frac{Ne^2}{4mc^2}A_0^2, \qquad (12)$$

where $\vec{P}$ is a momentum operator, $\vec{P} = \Sigma_i \vec{p}_i$. This is nothing more than the electromagnetic energy associated with the susceptibility of the medium. Considering E_2 as a function of ionic displacements, we can immediately identify it as an effective potential in the phonon coordinate whose gradient gives the force on the ions.

Our task is to show that this force is identical to that calculated by Eq. (9). This can be done quite generally making use of Floquet states. In the Floquet representation, the time-dependent wave function $\Psi(t)$ is expressed as

$$\Psi(t) = e^{-i\varepsilon_F t}\Phi_F(t), \qquad (13)$$

where the Floquet state $\Phi_F(t)$ is periodic with a period $T = (2\pi\omega)^{-1}$. It satisfies the equation

$$\mathcal{H}\Phi_F = \varepsilon_F\Phi_F, \qquad (14)$$

where $\mathcal{H} = H - i\partial/\partial t$. We can also express ε_F as the integral

$$\varepsilon_F = \frac{1}{T}\int_0^T dt \langle \Phi_F | \mathcal{H} | \Phi_F \rangle. \tag{15}$$

In fact this last equation is a variational principle for Φ_F and ε_F. This is the crucial point for making the connection. Since ε_F is stationary with respect to variations in Φ_F, the conditions for the Feynman-Hellman theorem apply and the derivative of ε_F with respect to a phonon coordinate may be calculated from the expectation value of $\partial\mathcal{H}/\partial q = \partial H/\partial q$,

$$\frac{d\varepsilon_F}{dq} = \frac{1}{T}\int_0^T dt \langle \Phi_F | \frac{\partial H}{\partial q} | \Phi_F \rangle. \tag{16}$$

The expectation value in the integrand is just the force calculated directly from the TDDFT equation of motion, Eq. (9).

IV. CALCULATIONAL DETAILS

Our calculations are based on the local-density approximation (LDA) density functional,[37] treating the four valence electrons of Silicon explicitly and using the Troullier-Martins pseudopotential.[38] We employ the real-time, real-space scheme which was developed by us.[32–34,39] The geometry is taken to be a simple cubic unit cell containing eight Si atoms (lattice constant $a = 10.26$ a.u.). The electron orbitals are represented by amplitudes on a Cartesian lattice. For the derivatives of the orbital wave functions, we use the nine-point difference formula for both the first and the second derivatives. The wave vectors for occupied orbitals are discretized on a three-dimensional lattice covering the Brillouin zone. The code first calculates the Kohn-Sham ground-state orbitals to initialize the time-dependent calculation. The time evolution is carried out by a fourth-order expansion that is stable for time steps smaller than $\Delta t = (2/9)^{1/2}(\Delta x)^2$ in atomic units, where Δx is the mesh spacing of the spatial lattice. In general, the results are insensitive to the choice of Δt provided the stability condition is satisfied. In the following calculations, we fix the positions of Si atoms and calculate the force acting on atoms according to the right-hand side of Eq. (9).

We now show some comparisons of the force calculation as a function of the number of lattice points. The numerical demands on the theory are more severe for photon energies above the direct band gap than for lower energies, so we make the comparison at a relatively high energy, $\hbar\omega = 4$ eV. Figure 2(a) shows the convergence of the force in [100] direction with respect to the number of grid points in the eight-atom unit cell. In this plot, the 24^3 subdivision is used for K-space grid. The calculated force changes sign between 12^3 and 16^3 lattices. It appears that a 16^3 lattice is sufficient to calculate the force to the needed accuracy of our semiquantitative theory. The sensitive to the coarseness of the wave number mesh is shown in Figs. 2(b) and 2(c), calculated using the 16^3 spatial lattice. It is important here to have a fine enough subdivision of points so that the absorptive part of the response does have large fluctuations due to the discretization. One sees that 8^3 mesh is quite inaccurate but there is convergence for the force at 16^3. The excitation energy shows some change from 16^3 to 24^3, so we adopt the finer
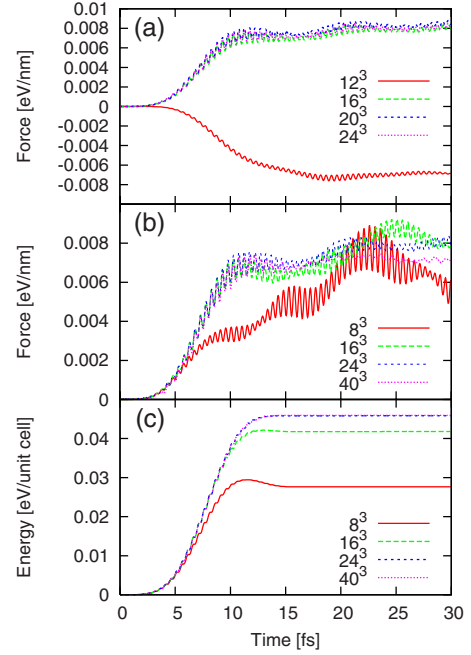

FIG. 2. (Color online) (a) Convergence of the force with respect to spatial lattice subdivision, (b) convergence of the force with respect to K-space grid, and (c) convergence of the excitation energy with respect to K-space grid.

mesh 24^3 for the calculations reported below. For the spatial mesh, we use the 16^3 lattice and a corresponding time step of $\Delta t = 0.08$ a.u. $\approx 2 \times 10^{-18}$ s. Denser lattices are possible in wave number lattice because the code has been parallelized by distributing the calculations for different wave vectors onto different processors. The system is evolved for a total time of 50–100 fs, which is sufficiently long to cover a cycle of vibration in the optical phonon. A typical computational wall time is 20 h with 32 nodes of four quad-core Opteron CPU (2.3 GHz), 512 cores in total.

V. RESULTS

A. Dielectric response

We first show dielectric properties of Si calculated with our LDA functional using the real-time method.[33] Figure 3 shows the comparison of the computed dielectric function with experiment. First we note that the LDA density functional gives a quite satisfactory account of the low-frequency dielectric function, predicting $\epsilon_{\text{LDA}} = 14$ at $\hbar\omega = 1$ eV compared to the experimental value $\epsilon_{\text{exp}} = 12$. However, as is well known the LDA theory underpredicts band gaps. In Si the calculated direct band gap is 2.4 eV compared to the experimental value of 3.3 eV. Since the mechanism to generate the coherent phonons is very dependent on the direct band gap, any comparison with experiment has to take into account the 0.9 eV shift. It is also of interest to see how closely the induced field follows the dielectric response when the exciting field has the form of a femtosecond-scale pulse. For the pulse excitation, we shall take the form [Eq. (7)] with a pulse duration of $T_p = 16$ fs. We show below the response to a
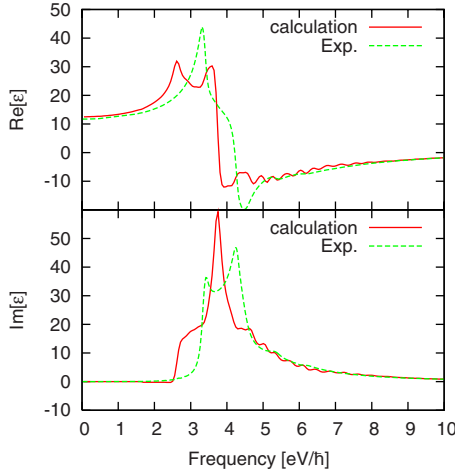
FIG. 3. (Color online) Dielectric function $\varepsilon(\omega)$ of crystalline Si, comparing the calculation based on the LDA DFT with experiment. Real and imaginary parts of ε are shown in upper and lower panels, respectively.

driving field whose strength A_{ext} is fixed to a peak electromagnetic wave intensity of $I = 10^{12}$ W/cm^2. This corresponds to a peak electric field strength of $\mathcal{E} = 2.7$ V/nm $= 0.005$ a.u. The total energy fluence per pulse is 0.08 J/cm^2. We note that the actual strength of the laser intensity should be estimated with A_{in} given by Eq. (8). Figure 4 shows the exciting electric field and the medium re-
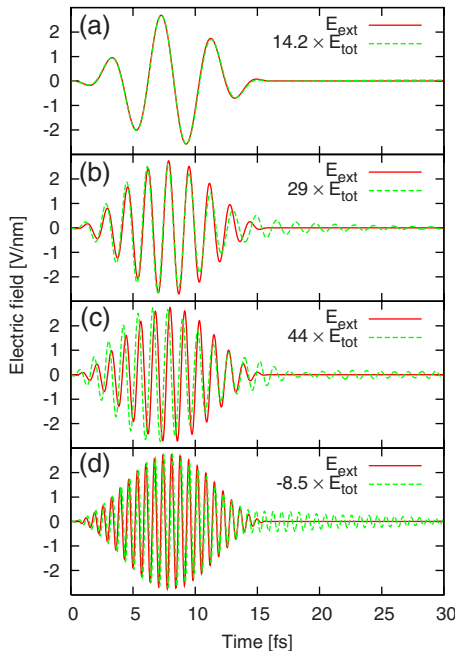

FIG. 4. (Color online) Dielectric response of Si. The red solid line shows the electric field associated with an external laser pulse of the form of Eq. (7), and the green dashed line shows the total electric field inside the crystal, scaled up by a factor S to facilitate the comparison. The panels show results for different laser frequencies. The peak intensity is the same ($I = 10^{12}$ W/cm^2) for all cases. (a) $\hbar\omega = 1.0$ eV, $S = 14$. (b) $\hbar\omega = 2.5$ eV, $S = 29$. (c) $\hbar\omega = 3.5$ eV, $S = 44$. (d) $\hbar\omega = 6.0$ eV, $S = -8.5$.

sponse for photon energies $\hbar\omega = 1.0$, 2.5, 3.5, and 6.0 eV. The red solid curve shows the driving field, $E_{ext} = -(1/c)dA_{ext}/dt$, and the green dashed curve shows the total field, $E = -(1/c)dA/dt$, including screening by the crystal. Panel (a) shows the two fields for $\hbar\omega = 1.0$ eV. We see that the total field is in phase with the driving field and goes to zero after the end of the pulse, as it must be when the photon energy is below the direct band gap. The total field has been scaled up by a factor of $\epsilon = 14$ to facilitate the comparison. Panel (b) shows the two fields for $\hbar\omega = 2.5$ eV, close to the direct band gap. Panel (c) shows the two fields for $\hbar\omega = 3.5$ eV. In this case, the frequency is near a maximum of the imaginary part of ϵ^{-1}. One can see that the driving field and total field are somewhat out of phase. The ratio between total and driving fields is about 44, which roughly coincides with the absolute value of the dielectric function at 3.5 eV, as seen from Fig. 3. For $\hbar\omega = 2.5$ and 3.5 eV cases, the oscillation persists after the end of the pulse, showing that electron-hole pairs having optical transition strength persist into the final state. Finally, panel (d) shows the two fields at $\hbar\omega = 6$ eV. This is beyond the main peak in the absorptive strength function, and the two fields are seen to have opposite phases.

The derivative of the dielectric function (or the susceptibility) with respect to the phonon coordinate should also be explicitly examined since it mediates the coupling in the adiabatic regime. The specific derivative, called the Raman tensor, was calculated with the same LDA density functional but using a quite different methodology in Ref. 31. The theoretical value was found to agree well with experimental data on incoherent phonon generation. With our methodology, we can compute the effective Raman tensor from the TDDFT calculation of the response to a laser pulse. The susceptibility tensor of the distorted lattice is expressed as [Eq. (4) of Ref. 31]

$$\chi_{xy}^{(1)} = 8Pq/a^2, \qquad (17)$$

where the phonon coordinate q is defined $\Delta\vec{R}(\pm) = \pm qa(0,0,1)$ in terms of the lattice constant a. The external field [Eq. (7)] with $\hbar\omega = 1$ eV is applied in the (110) direction and the response is measured by the induced polarizations in the same direction. The fractional change in the dielectric function as a function of the displacement q is obtained by comparing the applied and induced fields and is shown in Fig. 5. From this figure, one may extract the value of the Raman tensor, $d\chi_{xy}^{(1)}/dq$ at $q = 0$. This is 7.8, 25% higher than the measured value 6.8 ± 1 (Ref. 40) and 10% higher than the calculated value, 7.1, in Ref. 31.

B. Electron dynamics

In this section, we examine how the character of the electronic excitation changes as the laser frequency increases from below to above the direct band gap. Characteristics of the excitation as a function of time are shown for frequencies $\hbar\omega = 2.25$, 2.5, and 2.75 eV in Fig. 6. The top panel shows the total increase in energy in the unit cell, including both electronic excitation energy and the electromagnetic field energy. The red solid curve shows the results for a frequency
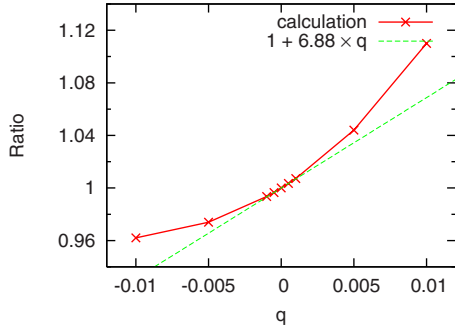
FIG. 5. (Color online) Dependence of the dielectric function on the phonon coordinate. The effective dielectric function is evaluated from the maximum strength ratio of the external and total electric fields. The pulse shape is taken of Eq. (7) with $\hbar\omega = 1$ eV.

below the band gap. Here the energy drops almost to zero after the pulse is over, as to be expected. The green dashed curve, corresponding to a frequency at the band gap, shows that some excitation energy remains after the end of the pulse, comparable in magnitude to the total energy at the peak. Finally, the blue dotted curve shows that above the gap the laser-electron interaction is highly dissipative, leaving a large excitation energy in the final state. The lower panel in the figure shows the number of excited electrons as a function of time. This is calculated by taking the overlaps of the time-dependent occupied orbitals with the initial state static orbitals as in Ref. 34. The results are qualitatively very similar to what we found for the energy. Below the direct band gap, the excited electron shows a peak during the pulse and then drops off to a very small value in the final state. At higher frequencies, the excitations remain in the final state and it is not possible to distinguish the real excitation from the virtual one during the pulse. In summary, one sees an adiabatic response below the gap switching rather abruptly to a strongly dissipative response above the gap.

We next show the electron dynamics in real space. Figure 7 shows the electron density in the plane of Fig. 1. The left panel shows the ground-state electron density, and the middle and right panels show the change in electron density from that in the ground state when the laser pulse of frequency $\hbar\omega = 2.5$ eV, close to the band gap, is irradiated. The external and the total electric fields for this laser pulse are
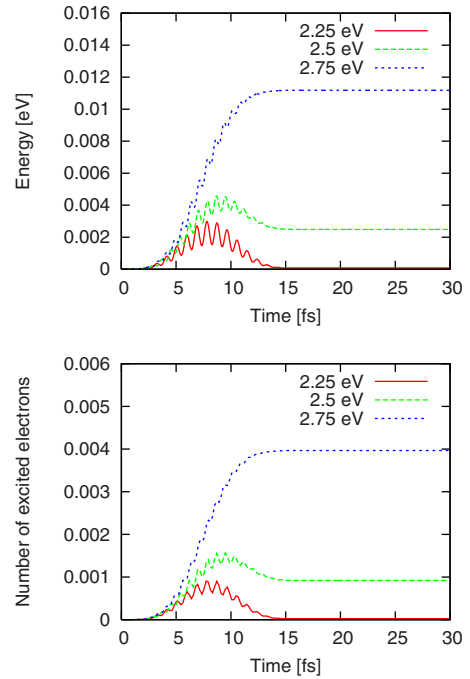

FIG. 6. (Color online) Excitation of the crystal during and after the pulse for several laser frequencies. The top panel shows the energy in the unit cell including electron-hole excitation energy and the electric field energy. The bottom panel shows the number of electron-hole pairs in the unit cell.

shown in the panel (b) of Fig. 4. The middle and right panels correspond to the time $t = 8.1$ fs and $t = 26.7$ fs, respectively. In the middle and right panels, red and blue indicate an increase or decrease in electron density, respectively. At $t = 8.1$ fs, the electric field is maximum and there is a strong virtual excitation of the electrons. In the middle panel of Fig. 7, a movement of electrons is seen in the bond connecting two Si atoms. At $t = 26.7$ fs, the external electric field ended. Since the ultrashort laser pulse includes frequency components above the direct band gap, there appear real electron-hole excitations. In the right panel of Fig. 7, one can see that the excitation results in a decreased density in the bond region and an increase near the Si atoms but away from the bond. One should note that the coloring of the middle and right figures are different by a factor of 40 to improve the
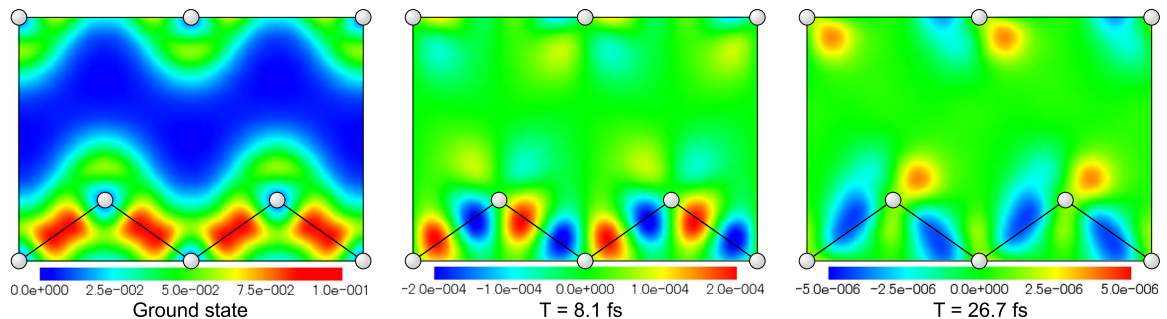

FIG. 7. (Color online) Left panel shows the ground-state electron density in the plane shown in Fig. 1. The middle and right panels show the change in the electron density from that in the ground state by the laser pulse corresponding to the panel (b) of Fig. 4. The middle panel corresponds to the time $t = 8.1$ fs and the right panel to the time $t = 26.7$ fs, respectively. In the middle and right panels, the red color indicates the increase in the electron density while blue color indicates the decrease.
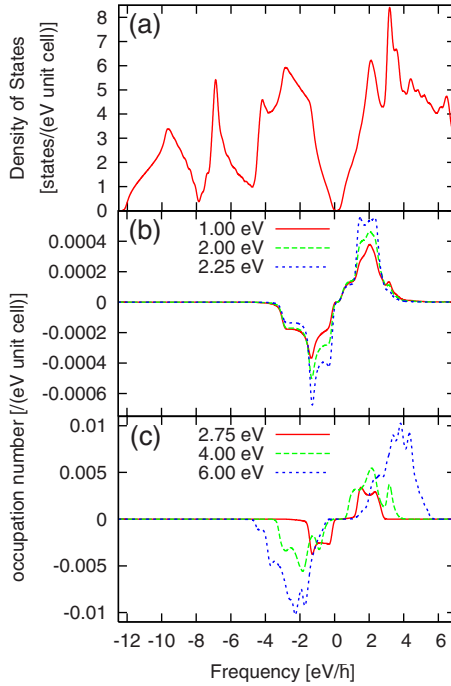
FIG. 8. (Color online) (a) Calculated electronic density of the state in Si. Change in occupation number (b) during and (c) after the laser pulse.
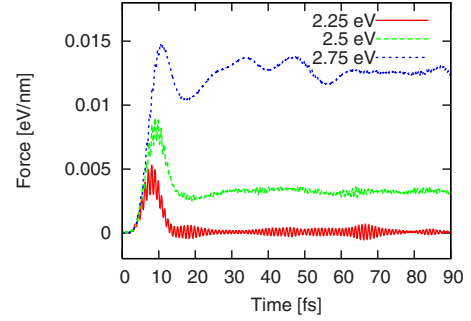

FIG. 9. (Color online) The force on the optical phonon coordinate for three laser frequencies: 2.25 eV (red solid); 2.5 eV (green dashed); and 2.75 eV (blue dotted).

visibility of the density change at time $t = 26.7$ fs.

We now examine in more detail the distribution of electrons and holes in the excitation. Figure 8(a) shows the calculated electronic density of states in Si as a function of energy with respect to the Fermi level. This was computed with the 24^3 mesh of wave numbers and smoothing the distribution with a Gaussian function. Note that the gap that is visible in Fig. 8(a) at $e - e_F \approx 0$ is indirect and much smaller than the direct gap. The change in the electron and hole occupation factors is shown for several frequencies in Figs. 8(b) and 8(c). Figure 8(b) shows the distribution at the peak of the pulse, for three frequencies below the gap. The excitations are virtual here, and the character of the distribution does not depend strongly on the frequency. As the frequency increases from 1.0 to 2.25 eV close to the direct band gap, the magnitude of the electron-hole excitation increases. This agrees with the increase in the real part of the dielectric function, as seen in Fig. 3. Figure 8(c) shows the distribution of electrons and holes in final state for three frequencies above the gap. One sees a progression of distributions with the highest frequency pulse exciting much deeper levels than the pulse just above the gap produces. We will see below that this will have some consequences for the coherent optical phonon.

C. Coupling to the lattice

We now turn to the force on the ions during and after the laser pulse. Figure 9 shows the calculated induced force for the same three frequencies spanning the direct gap that we examined earlier. Note that the ion positions are fixed in these calculations; the accelerations are small and the resulting displacements would be inconsequential.

The lowest frequency, shown by the red solid curve, gives a force envelope that follows the shape of the pulse intensity. This is just what one would expect from the adiabatic formula, Eq. (10). Here force is proportional to the square of the field strength averaged over a Floquet cycle of the wave function. One also sees high-frequency oscillations superimposed on the envelope of the curve. The frequency of these oscillations is twice the laser frequency, again as expected from the adiabatic formula.

The green dashed curve shows the force for a laser frequency of $\hbar\omega = 2.5$, nearly at the direct band gap. One still sees a large peak at 10 fs associated with instantaneous high-field intensity. However, there is a residual force after the end of the pulse which is rather constant with time. This is just what one expects for displacive mechanism. At this point, we have shown that TDDFT reproduces at a qualitative level the role of the two mechanisms. Beyond that, the relative sign associated with them can be extracted from the graph. The last case shown, $\hbar\omega = 2.75$, is 0.35 eV above the direct gap. Here the displacive mechanism is completely dominant, although one can still see an enhancement of the force during the pulse.

We now integrate the time-dependence force to get the lattice distortion associated with the phonon coordinate. In principle, the restoring potential for the lattice vibration is included in the evolution equations but the amplitude of the lattice displacement is extremely small and it would be problematic to treat its effects numerically. So for this part of the analysis we simply assume a harmonic restoring potential consistent with the observed optical phonon frequency, $f_{phonon} = 15.3$ THz. The results of the integration are shown in Fig. 10 for a Si atom depicted in Fig. 1. One sees that the amplitude increases greatly above the threshold. To analyze the characteristics of the coherent phonon more quantitatively, we fit the oscillation of the displacement in the time interval 40–90 fm to a cosine function similar to Eq. (1),

$$q(t) = -q_0 \cos(\omega_{ph} t + \phi) + \bar{q}, \tag{18}$$

where we choose $q_0 > 0$.

The results for the dependence of amplitude q_0, phase ϕ, and shift $\bar{q}$ on laser frequency are shown in Fig. 11. Below the direct-gap energy the phase is close to $\pi/2$ as expected for the Raman mechanism. The amplitude remains almost
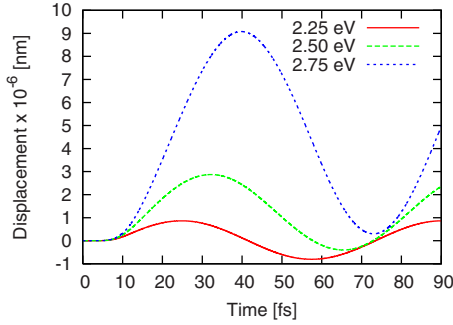
FIG. 10. (Color online) The displacement q along the optical phonon coordinate $\bar{q}=q[100]$ calculated by integrating the time-dependent force, assuming a harmonic restoring potential.

constant and the shift is vanishingly small in this frequency region, also consistent with the Raman mechanism. One sees a quite sharp drop from that value to $\phi=0$ as the direct gap is crossed, showing the transition to the displacive behavior. The amplitude and the shift also show a sudden increase across the direct gap. Several experimental measurements are also shown on the figure for the phase. Two of them[7,8] are in the Raman regime. The theory supports the results of Ref. 7, which reports a value close to $\pi/2$. The other measurement does not appear consistent with our theory or indeed with the other experiment. The phase has also been measured in the gap[6] region, shown by the square in Fig. 11(b). This point should be compared with the theory at the corresponding calculated gap energy, 2.4 eV. In both theory and experiment the phase has decreased from the Raman value but decrease seems larger for the experimental measurement. Both results are in a range where the mechanism is changing rapidly. All in all, we find the agreement quite satisfactory on a qualita-
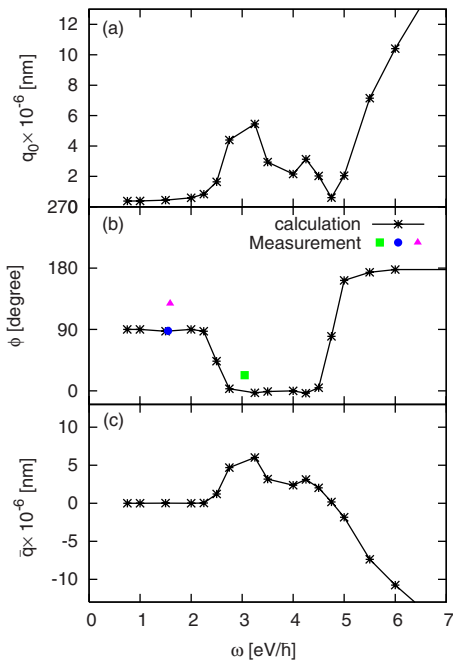

FIG. 11. (Color online) (a) The amplitude q_0, (b) the phase ϕ, and (c) the shift $\bar{q}$ of the phonon oscillation in Eq. (18) as a function of laser frequency.
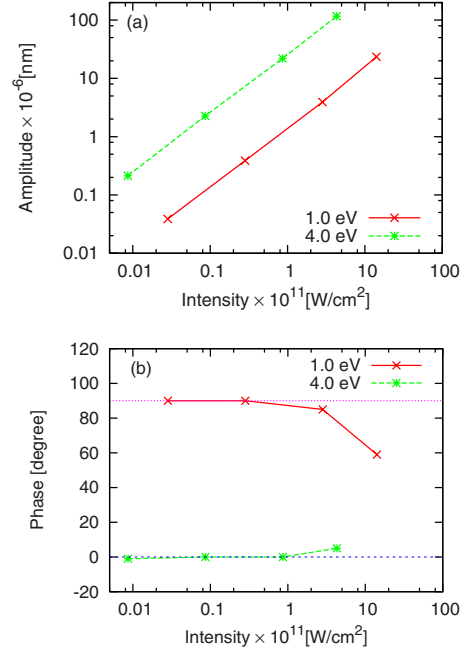

FIG. 12. (Color online) Characteristics of the phonon oscillation as a function of the laser intensity for two frequencies below and above the direct gap. The laser intensity A_{in} defined by Eq. (8) is used in this figure. (a) Amplitude of oscillation and (b) phase of oscillation.

tive level, particularly since the phase could have come out with an opposite sign ($\phi \approx \pi$).

At higher frequencies, the theoretical phase goes to zero as expected for the displacive mechanism. We find a change in the phase from $\phi \approx 0$ to $\phi \approx \pi$ between 4.5 and 5 eV. The amplitude also shows minimum around this frequency region, and the equilibrium position of the phonon coordinate $\bar{q}$ changes sign. In the case of laser frequency of 4.75 eV, a number of electron-hole pairs contribute destructively, yielding a small shift $\bar{q}$. We note that the phase ϕ may not be defined accurately at this frequency. Physically, this suggests that different electron orbitals are excited at the high frequency, and those orbitals have an opposite sign contribution to the displacive shift. In fact, we found earlier that the deeper hole excitations are favored at the higher frequencies.

D. Laser intensity dependence

We show in Fig. 12 the amplitude and phase of the coherent phonon as a function of the intensity of the laser pulse. The dependence on intensity is calculated for a frequency well below the gap (1.0 eV) and one well above (4.0 eV). One sees in Fig. 12(a) that the amplitude of the phonon is proportional to the laser intensity in both frequency regions. In the impulsive Raman mechanism which applied to 1.0 eV case, this is expected from the adiabatic, Eq. (10). In the displacive mechanism, this behavior is consistent with a process of electron-hole formation in one-photon absorption.

Figure 12(b) shows the phase of the phonon as a function of the laser intensity. At low intensity, the impulsive Raman mechanism is responsible for a laser pulse of 1.0 eV fre-

quency. However, as the laser intensity increases, real electron-hole excitation caused by multiphoton absorption becomes significant. This explains the reason why the phonon phase gradually decreases from $\pi/2$.

VI. DISCUSSION AND SUMMARY

We have derived and carried out a computational methodology to apply time-dependent density functional theory to laser-lattice interactions, taking as an example the excitation of coherent optical phonons by femtosecond-scale laser pulse in silicon. The theory merges with the macroscopic theory in the adiabatic limit, where the process is controlled by the dielectric response function. Our TDDFT calculation goes beyond the previous work in that it is the first *ab initio* calculation extending to the nonadiabatic frequency domain. However, there are a number of limitations of TDDFT that should be kept it mind. The quality of the calculated results is limited by the accuracy of the energy functional which relies on the adiabatic local-density approximation. As is well known, the local-density approximation significantly underestimates the band gap of insulators and semiconductors. The behavior of the dielectric function around the band gap, which is very important for a quantitative description of the generation of coherent phonon, is not described accurately, as seen from Fig. 3. While the shift of the direct band gap is a well-known problem of the LDA functional that might be ameliorated with a different functional, the fact that there is absorption below the direct gap is beyond the scope of the theory. We also note that the TDDFT does not treat the damping of excitations by electron-electron collisions. The lifetime of the displacive excited state was found to be significant to the coherent phonon phase in Ref. 7, and that can only be calculated with inclusion of collisions.

It is of interest to compare the *ab initio* results with the predictions of the much simpler SKM model,[30] which also spans the frequency domain from the adiabatic to the displacive regions. In that model, the phase is given by $\phi = \arctan(\Omega \varepsilon_r'/2\varepsilon_i)$. Taking the dielectric function $\varepsilon = \varepsilon_r + i\varepsilon_i$ from the TDDFT calculation (Fig. 3), we find a predicted ϕ shown by the green line in Fig. 13. One sees that there is very sharp drop from $\phi = \pi/2$ just above the direct band gap at 2.4 eV. The phase is entirely dominated by upper band displacive mechanism for all higher frequencies. This is compared with our calculated results, shown here as black
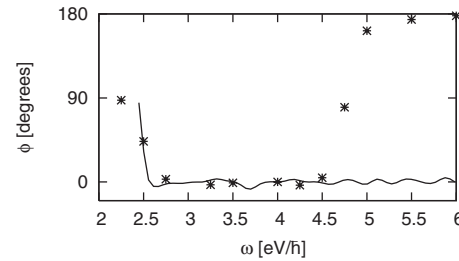

FIG. 13. Comparison of the predicted coherent phonon phase ϕ for the TDDFT and the SKM model with the dielectric function of the TDDFT.

circles. It appears that the SKM model is consistent with the full TDDFT calculation in the threshold region, although it is not clear from the sampling of frequency points how sharply the phase changes in the TDDFT. At the higher frequencies where more bands come into play, the SKM model is obviously inconsistent with the full calculation.

There are several areas where the theory can be refined or developed further. We have only given an approximate treatment of the laser field in the solid, generating it by the numerical expedient of adding the external field $\vec{A}_{\text{ext}}$ to Eq. (5). A more complete theory would treat the propagation of the electromagnetic pulse through the medium. The electric field part of the vector potential $\vec{A}$ is generated by the magnetic term $\vec{\nabla} \times \vec{\nabla} \times \vec{A}$ in the wave equation, and that would act as the source of the field. Certainly, at the higher frequencies where absorption is important the propagation should be treated explicitly, as has been done in Ref. 41. Once the propagation has been incorporated into the theory, it will be possible to treat the amplitudes of the coherent phonon above the transition region in a more quantitative way.

[1] S. De Silvestri, J. G. Fujimoto, E. P. Ippen, E. B. Gamble, Jr., L. R. Williams, and K. A. Nelson, Chem. Phys. Lett. **116**, 146 (1985).

[2] K. Ishioka, M. Hase, and M. Kitajima, Appl. Phys. Lett. **89**, 231916 (2006).

[3] A. D. Savvin, A. A. Lanin, A. A. Voronin, A. B. Fedotov, and A. M. Zheltikov, Opt. Lett. **35**, 919 (2010).

[4] T. K. Cheng, S. D. Brorson, A. S. Kazeroonian, J. S. Moodera, G. Dresselhaus, M. S. Dresselhaus, and E. P. Ippen, Appl. Phys. Lett. **57**, 1004 (1990).

[5] G. C. Cho, W. Kütt, and H. Kurz, Phys. Rev. Lett. **65**, 764 (1990).

[6] M. Hase, M. Kitajima, A. Constantinescu, and H. Petek, Nature (London) **426**, 51 (2003).

[7] D. M. Riffe and A. J. Sabbah, Phys. Rev. B **76**, 085207 (2007).

[8] K. Kato, A. Ishizawa, K. Oguri, K. Tateno, T. Tawara, H. Gotoh, M. Kitajima, and H. Nakano, Jpn. J. Appl. Phys. **48**, 100205 (2009).

[9] A. Hussain and S. R. Andrews, Phys. Rev. B **81**, 224304 (2010).

[10] M. Hase, K. Ishioka, J. Demsar, K. Ushida, and M. Kitajima,

Phys. Rev. B **71**, 184301 (2005).

[11] M. Hase, K. Mizoguchi, H. Harima, S. Nakashima, M. Tani, K. Sakai, and M. Hangyo, Appl. Phys. Lett. **69**, 2474 (1996).

[12] A. M.-T. Kim, C. A. D. Roeser, and E. Mazur, Phys. Rev. B **68**, 012301 (2003).

[13] K. Sokolowski-Tinten, C. Blome, J. Blums, A. Cavalleri, C. Dietrich, A. Tarasevitch, I. Uschmann, E. Förster, M. Kammler, M. Horn-von-Hoegen, and D. von der Linde, Nature (London) **422**, 287 (2003).

[14] O. V. Misochko, K. Ishioka, M. Hase, and M. Kitajima, J. Phys.: Condens. Matter **19**, 156227 (2007).

[15] S. L. Johnson, P. Beaud, C. J. Milne, F. S. Krasniqi, E. S. Zijlstra, M. E. Garcia, M. Kaiser, D. Grolimund, R. Abela, and G. Ingold, Phys. Rev. Lett. **100**, 155501 (2008).

[16] C. J. Brennan and K. A. Nelson, J. Chem. Phys. **107**, 9691 (1997).

[17] A. Melnikov, I. Radu, U. Bovensiepen, O. Krupin, K. Starke, E. Matthias, and M. Wolf, Phys. Rev. Lett. **91**, 227403 (2003).

[18] S. B. Fleischer, B. Pevzner, D. J. Dougherty, H. J. Zeiger, G. Dresselhaus, M. S. Dresselhaus, E. P. Ippen, and A. F. Hebard, Appl. Phys. Lett. **71**, 2734 (1997).

[19] D. Polli, M. R. Antognazza, D. Brida, G. Lanzani, G. Gerullo, and S. De Silvestri, Chem. Phys. **350**, 45 (2008).

[20] J. Takahashi, Y. Kawabe, and E. Hanamura, Opt. Express **12**, 1185 (2004).

[21] T. Dekorsy, G. C. Cho, and H. Kurz, Top. Appl. Phys. **76**, 169 (2000).

[22] R. Merlin, Solid State Commun. **102**, 207 (1997).

[23] Y.-X. Yan, E. B. Gamble, Jr., and K. A. Nelson, J. Chem. Phys. **83**, 5391 (1985).

[24] R. Loudon, Proc. R. Soc. London, Ser. A **275**, 218 (1963); Adv. Phys. **13**, 423 (1964).

[25] H. Smith, Philos. Trans. R. Soc. London, Ser. A **241**, 105 (1948).

[26] H. J. Zeiger, J. Vidal, T. K. Cheng, E. P. Ippen, G. Dresselhaus, and M. S. Dresselhaus, Phys. Rev. B **45**, 768 (1992).

[27] R. Scholz, T. Pfeifer, and H. Kurz, Phys. Rev. B **47**, 16229 (1993).

[28] A. V. Kuznetsov and C. J. Stanton, Phys. Rev. Lett. **73**, 3243 (1994).

[29] G. A. Garrett, T. F. Albrecht, J. F. Whitaker, and R. Merlin, Phys. Rev. Lett. **77**, 3661 (1996).

[30] T. E. Stevens, J. Kuhl, and R. Merlin, Phys. Rev. B **65**, 144304 (2002).

[31] S. Baroni and R. Resta, Phys. Rev. B **33**, 5969 (1986).

[32] Y. Shinohara, Y. Kawashita, J.-I. Iwata, K. Yabana, T. Otobe, and G. F. Bertsch, J. Phys.: Condens. Matter **22**, 384212 (2010).

[33] G. F. Bertsch, J. I. Iwata, A. Rubio, and K. Yabana, Phys. Rev. B **62**, 7998 (2000).

[34] T. Otobe, M. Yamagiwa, J.-I. Iwata, K. Yabana, T. Nakatsukasa, and G. F. Bertsch, Phys. Rev. B **77**, 165104 (2008).

[35] S.-I. Sawada, A. Nitzan, and H. Metiu, Phys. Rev. B **32**, 851 (1985).

[36] X. Li, J. C. Tully, H. B. Schlegel, and M. J. Frisch, J. Chem. Phys. **123**, 084106 (2005).

[37] J. P. Perdew and A. Zunger, Phys. Rev. B **23**, 5048 (1981).

[38] N. Troullier and J. L. Martins, Phys. Rev. B **43**, 1993 (1991).

[39] K. Yabana and G. F. Bertsch, Phys. Rev. B **54**, 4484 (1996).

[40] J. Wagner and M. Cardona, Solid State Commun. **48**, 301 (1983), as quoted in Ref. 31.

[41] J. R. Peñano, P. Sprangle, B. Hafizi, W. Manheimer, and A. Zigler, Phys. Rev. E **72**, 036412 (2005).